Comparative Studies of Microtubule Mechanics with Two Competing Models Suggest Functional Roles of Alternative Tubulin Lateral Interactions

Zhanghan Wu,[†] Eva Nogales,[‡§] and Jianhua Xing[†]

[†]Department of Biological Sciences, Virginia Tech, Blacksburg, Virginia; [‡]Lawrence Berkeley National Laboratory, Berkeley, California; and [§]Howard Hughes Medical Institute and Department of Molecular Cell Biology, University of California, Berkeley, California

Supplemental Information

Supplemental Methods

Model:

As discussed in the main text, we used a coarse-grained modeling framework that treated α and β tubulin monomers as rigid bodies (rods) connected by elastic springs. Moreover, we assumed that the monomers were chained together along the longitudinal direction in each protofilament (PF). This assumption is consistent with the model of VanBuren et al.(1) However, in our case a monomer is more than just the vector used in the work of VanBuren et al. The rod (monomer) can rotate along its long axis to account for heterogeneous lateral interactions between tubulins. To describe the behavior of the microtubules (MTs), we first needed to define the spatial position and orientation of each monomer. In general a rigid body has 6 degrees of freedom to specify its position and orientation. However, the connected rod model restrains the number of degrees of freedom. For convenience of mathematical formulation of the model, we used two sets of coordinate frames. Each tubulin monomer is treated as a three-dimensional rigid body, and thus has an intrinsic coordinate frame. Therefore one can specify the spatial and orientational coordinates of a monomer by comparing its intrinsic coordinate frame with the laboratory fixed frame, or with the intrinsic frame of the previous monomer on the same PF. Below we explains the procedure in detail.

For the *j*-th PF, one first needs 3 coordinates ($x_{0,j}$, $y_{0,j}$, $z_{0,j}$) in the laboratory frame to specify the spatial coordinate of the minus end of the first α-tubulin relative to the laboratory frame. Then the spatial coordinate of the plus end of the α-tubulin is given by

($x_{1,j}$, $y_{1,j}$, $z_{1,j}$). One also needs another coordinate $\psi^L_{1,j}$ to describe the rotation along the rod long axis relative to the laboratory frame. Alternatively, one can use the relative coordinates ($L_{1,j}$, $\theta_{1,j}$, $\varphi_{1,j}$, $\psi_{1,j}$), where $L_{1,j}$ is the modulus of the vector $\boldsymbol{r}_{1,j}$ =($x_{1,j} - x_{0,j}$, $y_{1,j} - y_{0,j}$, $z_{1,j} - z_{0,j}$), and ($\theta_{1,j}$, $\varphi_{1,j}$, $\psi_{1,j}$) are a set of angles defined in Figure 1d of the main text to determine the orientation of the monomer with respect to the previous monomer—the laboratory frame in this case. The next tubulin monomer, a β-tubulin, has its minus end at ($x_{1,j}$, $y_{1,j}$, $z_{1,j}$), and can be similarly described by a set of relative coordinates ($L_{2,j}$, $\theta_{2,j}$, $\varphi_{2,j}$, $\psi_{2,j}$). The remaining monomers can be described in a similar way. The transformation between the coordinates in the laboratory frame, $(x_{i,j}, y_{i,j}, z_{i,j}, \psi^L_{i,j})$, and the relative coordinates ($L_{i,j}$, $\theta_{i,j}$, $\varphi_{i,j}$, $\psi_{i,j}$) is given by

$$\begin{aligned} x_{i,j} &= x_{i-1,j} + L_{i,j}\sin\theta_{i,j}\cos\phi_{i,j}, \\ y_{i,j} &= y_{i-1,j} + L_{i,j}\sin\theta_{i,j}\sin\phi_{i,j}, \\ z_{i,j} &= z_{i-1,j} + L_{i,j}\cos\theta_{i,j}, \\ \psi^L_{i,j} &= \psi^L_{i-1,j} + \psi_{i,j}. \end{aligned} \tag{S1}$$

and for the inverse transformation,

$$\begin{aligned} L^2_{i,j} &= (x_{i,j} - x_{i-1,j})^2 + (y_{i,j} - y_{i-1,j})^2 + (z_{i,j} - z_{i-1,j})^2 \\ \theta_{i,j} &= \arccos((z_{i,j} - z_{i-1,j}) / L_{i,j}) \\ \phi_{i,j} &= \begin{cases} \arcsin((y_{i,j} - y_{i-1,j}) / L2), & \text{if } 0 \le x_{i,j} - x_{i-1,j}; \\ \pi - \arcsin((y_{i,j} - y_{i-1,j}) / L2), & \text{if } x_{i,j} - x_{i-1,j} < 0. \end{cases} \\ \psi_{i,j} &= \psi^L_{i,j} - \psi^L_{i-1,j}. \end{aligned} \tag{S2}$$

where $L2^2 = (x_{i,j} - x_{i-1,j})^2 + (y_{i,j} - y_{i-1,j})^2$. The energy terms are functions of the relative coordinates between monomers. Following VanBuren et al.(1), one can introduce an auxiliary coordinate Φ to describe deviation of the bending angle between the (i-1)-th and i-th monomers within the j-th PF from the preferred value,

$$\Phi_{i,j} = \arccos(l_{i-1,j}l_{i,j} + m_{i-1,j}m_{i,j} + n_{i-1,j}n_{i,j}), \tag{S3}$$

where the terms *l, m,* and *n* are the direction cosines given by

$$l_{i,j} = \frac{x_{i,j} - x_{i-1,j}}{L_{i,j}}, m_{i,j} = \frac{y_{i,j} - y_{i-1,j}}{L_{i,j}}, n_{i,j} = \frac{z_{i,j} - z_{i-1,j}}{L_{i,j}}. \tag{S4}$$

Having defined the position of the monomers through longitudinal interactions, one can then derive the quantities describing the lateral interactions between 2 monomers (*i', j-1*) and (*i, j*),: the distance between two monomers d_{ij}, the shift angle between two monomers Φ_s, and the rotational angle γ_r (see Figure 1e in the main text). The term *d* is defined as

$$\begin{aligned} d_{i,j} &= \left\| \mathbf{r}_{i,j} - \mathbf{r}_{i',j-1} \right\| \\ &= ((x^c_{i,j} - x^c_{i',j-1})^2 + (y^c_{i,j} - y^c_{i',j-1})^2 + (z^c_{i,j} - z^c_{i',j-1})^2)^{1/2}. \end{aligned} \tag{S5}$$

where $x^c_{i,j} = \frac{x_{i,j} + x_{i-1,j}}{2}$ and the others have the similar definitions. The shift and rotational angles Φ_s and γ_r are defined also from the global coordinates.

$$\begin{aligned} \Phi_s^{i,j} &= \arccos(l^{lat}{}_{i,j} l^{lat}{}_{i,j-1} + m^{lat}{}_{i,j} m^{lat}{}_{i,j-1} + n^{lat}{}_{i,j} n^{lat}{}_{i,j-1}), \\ \gamma_r^{i,j} &= \psi^L_{i,j} - \psi^L_{i,j-1}. \end{aligned} \tag{S6}$$

where the definitions of l^{lat}, m^{lat}, and n^{lat} are similar to those in Eq. (S4) except that L_{ij} is replaced by d_{ij}. The details can be understood from Figure 1 in the main text and Figure S1. These relative coordinates can be used to define the energy terms.

Energy terms and parameter estimations:

From the Young's Modulus measurements of MT and the second moment of inertia, one can derive the values of k_{long} and k_{lat} (1). The Yong's Modulus can be determined based on the rigidity EI. Table S1 summarizes some of the experimental results (2-11). The

measured rigidity of MT has a very wide range, and thus so does the Young's Modulus. Binding of MT associated proteins may contribute to the diversity. In our studies we used data from (12, 13) which were obtained under similar experimental conditions as those we used in our simulations. Furthermore, we found that most of the spring constants had little effect to the problems we are addressing (see Figure 3). Specifically, the Young's Modulus E can be derived from

$$\begin{aligned} E &= \frac{EI}{I} \\ I &= \frac{\pi}{4}(r_{outer}^4 - r_{inner}^4) \\ r_{inner} &= 8.4 \text{ nm} \\ r_{outter} &= r_{inner} + d_t \end{aligned} \tag{S7}$$

Choosing an effective thickness of MT wall d_t =1.54 nm (12)*, one has

$$I = \frac{\pi}{4}(r_{outer}^4 - r_{inner}^4) = 8.012 \times 10^{-33} \text{m}^4 \tag{S8}$$

$$E = \frac{EI}{I} = \begin{cases} \dfrac{1 \sim 2.5 \times 10^{-24} \text{Nm}^2}{3.757 \times 10^{-33} \text{m}^4} \\ \dfrac{3 \sim 9 \times 10^{-24} \text{Nm}^2}{3.757 \times 10^{-33} \text{m}^4} \end{cases} = \begin{cases} 0.266 \sim 0.665 \times 10^9 \text{ N/m}^2 & \text{Taxol MT} \\ 0.799 \sim 2.396 \times 10^9 \text{ N/m}^2 & \text{Pure MT} \end{cases} \tag{S9}$$

In this work the Young's Modulus was chosen to be 0.665GPa (for Taxol MT) in order to be consistent with most of the experiments reported, especially AFM experiments (12, 13).

The spring constant related to a given Young's Modulus can then be derived from

* Notice that the effective thickness and monomer size discussed below are not equivalent to the geometric size of a monomer. See (1) for more detailed discussions.

$$k = \frac{EA}{L_0}. \tag{S10}$$

where A is the cross section area perpendicular to the direction of force, and L_0 is the original length along the direction of force. In our case, they are cross sections of longitudinal/lateral interaction and length/width of monomer, respectively. The effective size of monomer is 5.15 nm x 4 nm x 1.54 nm (12). Therefore, one can determine the values of k_{long} and k_{lat},

$$k_{lat} = \frac{0.665\ \text{GPa} \times (4\text{nm} \times 1.54\text{nm})}{5.15\text{nm}} = 0.795417\ \text{GPa} \cdot \text{nm} \tag{S11}$$

$$k_{long} = \frac{0.665\ \text{GPa} \times (5.15 \times 1.54)}{4} = 1.31853\ \text{GPa} \cdot \text{nm} \tag{S12}$$

or, in the unit of k_BT (at T = 300 K).

$$\begin{aligned} k_{lat} &= 0.795417\ \text{GPa} \cdot \text{nm} \\ &= 96.73 \frac{k_B T}{\text{dimer} \cdot nm^2} \end{aligned} \tag{S13}$$

$$\begin{aligned} k_{long} &= 1.31853\ \ \text{GPa} \cdot \text{nm} \\ &= 160.347 \frac{k_B T}{\text{dimer} \cdot nm^2} \end{aligned} \tag{S14}$$

The bending spring constant can be determined in the following way: the energy stored in the bending dimer is 2.5~3 k_BT(1, 14). One can then use

$$E_{bend} = \frac{1}{2} \kappa_{bend} \Phi^2 \tag{S15}$$

to determine the bending constant. The maximum bending angle is ~22^0 (0.384 rad)(15). One then has

$$k_{bend} = \frac{2.5\ \mathrm{k_B T/dimer} \times 2}{(0.384\ \mathrm{rad})^2} = 34 \frac{\mathrm{k_B T}}{\mathrm{dimer} \cdot\ \mathrm{rad}^2} \tag{S16}$$

The shear modulus is estimated to be 48 MPa from (16) (MD) and 1.4+/-0.4MPa from (17, 18) (AFM Exp). The shift energy has the form

$$E_{\mathrm{shift}} = \frac{3Lh}{2p} Gx^2 = \frac{3Lh}{2p} Gp^2 \tan^2 \Phi_s = \frac{3Lph}{2} G \tan^2 \Phi_s = \frac{1}{2} k_{shift} \tan^2 \Phi_s \tag{S17}$$

Therefore

$$k_{\mathrm{shift\_tube}} = 3LphG \tag{S18}$$

where G is the shear modulus (we use 10 MPa in our simulation), L is the length of a monomer (4 nm), p is the effective width between lateral monomers (5.15 nm), h is the effective thickness of the MT wall (1.54 nm). The value of k_{shift_tube} of tube bond is

$$\begin{aligned} k_{shift\_Tube} &= 3 \times 4nm \times 5.15nm \times 1.54nm \times 0.01GPa \\ &= 115.75 \frac{k_B T}{\mathrm{dimer}} \end{aligned} \tag{S19}$$

For G being 1MPa - 50Mpa, the corresponding k_{shift_tube} is 11 ~ 580 k_BT/dimer.

No experimental data exists to estimate the value of k_{shift} for the sheet bond, so we examined the effect of changing the value within the range k_{shift_sheet} = 10 ~ 100 k_BT/dimer (see Figure3 In the main text). For simplicity, we assumed that the shear properties for each monomer were symmetric with respect to the longitudinal and lateral directions.

Experimental information of the torsion energy for longitudinal interactions and rotational energy for lateral interactions is also absent. These energy terms are closely

related because rotation of a monomer changes the torsion of the PF directly. We also examined values of these terms within a range (see Figure3 in the main text). Based on the data fitting of both AFM experiments and structure information from (19), one set of values of the spring constants for these two energy terms is

$$k_{tor} = 10\frac{\mathrm{k}_B\mathrm{T}}{\mathrm{dimer}\cdot\mathrm{rad}^2} \tag{S20}$$

$$\begin{aligned} k_{rot\_sheet} &= 10\frac{\mathrm{k}_B\mathrm{T}}{\mathrm{dimer}\cdot\mathrm{rad}^2} \\ k_{rot\_tube} &= 50\frac{\mathrm{k}_B\mathrm{T}}{\mathrm{dimer}\cdot\mathrm{rad}^2} \end{aligned} \tag{S21}$$

Bilinear gap analysis:

The "gap" in the force-indentation (F-I) curves of Schapp et al. (12) can be characterized by two quantities: the kink position Γ and the gap width d_{gap}. The gap separates the quasilinear response into two regions before the MT is ultimately "crashed". Figure S2 schematically shows our method to calculate these two quantities. The kink position is defined as the first positions where the stepping behavior happens. The gap width is defined as the width when the second linear region starts to catch up the height of the first linear region. Below we discuss how the F-I curve is generated in our simulations.

At each step the AFM cantilever position changes from ($z_{AFM} - \Delta z_{AFM}$) to z_{AFM}. Correspondingly, the MT wall changes its position from ($z_{MT} - \Delta z_{MT}$) to z_{MT}. z_{AFM} and z_{MT} are defined as the change in position of the cantilever and the MT wall, respectively. More details can be found in Figure S7. Notice that the AFM cantilever is elastic (with spring constant of 0.03N/m as in (12)), so in general $\Delta z_{AFM} \neq \Delta z_{MT}$. Therefore, with the assumption that the AFM cantilever always touches the MT, the AFM cantilever

deformation is given by $z_S = z_{AFM} - z_{MT}$. In their experiments, Schmitt et al measured z_{AFM} and z_s experimentally, and then reported the measured force as a function of Δz_{MT}.

In our simulations, the quantity Δz_{MT} was externally controlled at every step. As discussed below, some calibration is needed. The force balance relation gives $F = k_S z_S = \frac{\partial(U(z_{MT}))}{\partial z_{MT}}$, or in the discretize form,

$$F(z_{MT}) = k_S \cdot (z_{S_{i-1}} + \Delta z_S) = \frac{U(z_{MT}) - U(z_{MT} - \Delta z_{MT})}{\Delta z_{MT}} \quad \text{(S22)}$$

Where z_{Si-1} is the cantilever deformation at the previous step (index i indicates the current step). However, the above force-balance assumption breaks down in the case where $\frac{U(z_{MT}) - U(z_{MT} - \Delta z_{MT})}{\Delta z_{MT}} < 0$ (region 2 in Figure 1i). With a finite rate of cantilever displacement, the system is out of mechanical equilibrium. Notice that the cantilever movement at each step is constrained to be $-\Delta z_{MT} < \Delta z_S < \frac{F_{\max}}{k_S} - z_{S_{i-1}}$. Within this region, the nonequilibrium force is given by

$$F(z_{MT}) = F(z_{MT} - \Delta z_{MT}) - k_S \cdot \Delta z_{MT} \quad \text{(S23)}$$

Here we assumed that the change of MT wall deformation was rate limiting and the AFM tip always touched the MT wall. This method becomes less accurate when large amount of breakage events take place as the MT wall deformation becomes too large. In the highly nonlinear region (region 4 in Figure2b of the main text), the interaction between AFM tip and MT wall in the experiments becomes dramatic, and our simulations no longer represent the same conditions as in experiments.

As mentioned in the main text, with the original data of F as a function of z_{AFM}, and the information of the cantilever moving rate, one can, in principle, reconstruct the free energy profile from the experimental data using a procedure developed for analyzing single molecule force measurements based on the Jarzynski equality (20).

Supplemental Results:

The effects of moving AFM tip between and along MT PFs:

Besides changing the size of AFM tip radius and the MT length, another set of simulations that could be directly tested experimentally is to change the position of the AFM tip by moving it across, from one protofilament to the next (Figure S6a&b), or along a protofilament (the MT longitudinal direction) (Figure S6e). MTs are polymers of α- and β-tubulin dimers. Dimers polymerize end to end along PFs, which associate laterally into hollow cylindrical filaments. Therefore, the wall of MTs is not a smooth "wall". There are in fact "bumps" along both the longitudinal (z) and lateral directions (x). We find that the "bumps" along the PFs result in no observable difference on both linear and quasi-linear responses, but the ones formed between PFs do have effects on both kinds of mechanical responses.

Figure S6c plots the linear response of the MT wall to the AFM tip while the tip starts from different *x* direction (Figure S6a) and then pushes the wall along the negative *y* direction. Starting from position *x = 0* nm, the spring constant κ slightly decreases as the x varies away from this point. But the decreasing trend stops temporarily at $x \approx 3.5$ nm and then decrease again at similar rate as that observed between x = 0 and 3.5 nm. The decreasing trend stops again at about 4.5 nm. The slope increases about 0.005 N/m and

reaches maximum at 5.5 nm position. After that, the line drops quickly down to about 0.01 N/m. In these simulations, we used an AFM tip radius R = 15 nm. If we take a closer look of the MT structure (Figure S6), we find that the contact point of the AFM tip on the MT wall is at the center of PF number 1 (see Figure S6) for x = 0. When the tip moves away, the tip center shifts away from PF 1. This decreases the effective spring constant a little bit, as observed in Figure S6c for x=0~3.5 nm. At x~3.5 nm, the tip contacts PF 2 and moves away from PF 1. That explains why κ increases at that point. The decreasing of κ afterwards is due to similar reasons, as the trend repeats. The last increase before x = 5.5 nm is due to the tip contacting PF1, PF2 and even part of PF3 (note that the tip radius R = 15 nm). That results in a big jump of linear response on tip pressure. For x>5.5 nm, since the tip moves away from the whole MT, κ eventually decreases to zero as the tip finally looses contact with the MT wall.

The value of Γ (Figure S6d), on the other hand, increases from 3.5 to 5 nm when x changes from 0 to 3.8 nm and then stays at 5 nm level for a further displacement of up to 4 nm. This step corresponds to the monomer size (~4 nm in diameter). The system has this kind of response pattern because there are "bumps" between PFs on the MT wall, about 4 nm apart. This changes the gap position as the force exerting pattern changes when the tip moves from the center to the edge of the wall, crossing the "bumps" periodically.

Figure S6e-g plots similar responses for the AFM tip at different starting positions along the longitudinal direction (z). As expected, the linear response is stable before the boundary effect shows up, and then drops to zero as the tip moves to the upper edge of the MT and loses contact to the MT wall eventually (Figure S6f). The kink position plot

has a correlated response. When the spring constant decreases, the kink position increases correspondingly. The soft end of MT wall spread the force to more monomers and effectively delays the events of bond transitions, which is represented by a kink in the force-indentation curve.

The L1 Model fails to predict the gap behavior consistently:

To investigate the possibility that L1 model is capable of generating the experimental gap behavior in the AFM experiments, we performed large amount of simulations using the L1 model. The results suggest that the L1 model fails to predict the gap behavior consistently, under various conditions and different adjustable parameters.

As shown in the main text, the L1 model does not give a continuous gap behavior when the AFM tip radius is changed. This result indicates that it should be possible to discriminate between the L1 and L2 models experimentally. In this section, we further examine the L1 model behavior to validate our conclusion.

The estimated lateral binding free energy is -3.2~-5.7 k_BT (21). To more thoroughly investigate the L1 model, we performed simulations using different lateral binding free energies. The results show (Figure S4 & S9) that the L1 model cannot reproduce the gap behavior robustly. The gap appears either at an indentation larger than observed, or never happens. This observation further questions the ability of the L1 model to explain the quasi-linear behavior in a self-consistent way, while the experimental observations are highly repeatable (12).

L2 model reproduces the tip structure at disassemble stage

As shown in Figure S8, L2 model can easily reproduce the horn like tip structure when the MT is at disassembly stage. The figure shows a typical configuration from L2 model. The structure is consistent with the one observed in the experiments and previous L1 models (1, 22, 23).

References

1. VanBuren, V., L. Cassimeris, and D. J. Odde. 2005. Mechanochemical model of microtubule structure and self-assembly kinetics. Biophys J 89:2911-2926.
2. Cassimeris, L., D. Gard, P. T. Tran, and H. P. Erickson. 2001. XMAP215 is a long thin molecule that does not increase microtubule stiffness. Journal of Cell Science 114:3025-3033.
3. Felgner, H., R. Frank, and M. Schliwa. 1996. Flexural rigidity of microtubules measured with the use of optical tweezers. J. Cell Sci. 109:509-516.
4. Janson, M. E., and M. Dogterom. 2004. A Bending Mode Analysis for Growing Microtubules: Evidence for a Velocity-Dependent Rigidity. 87:2723-2736.
5. Kikumoto, M., M. Kurachi, V. Tosa, and H. Tashiro. 2006. Flexural Rigidity of Individual Microtubules Measured by a Buckling Force with Optical Traps. Biophys. J. 90:1687-1696.
6. Kurachi, M., M. Hoshi, and H. Tashiro. 1995. Buckling of a single microtubule by optical trapping forces: Direct measurement of microtubule rigidity. Cell Motility and the Cytoskeleton 30:221-228.
7. Kurz, J. C., and R. C. Williams, Jr. 1995. Microtubule-associated proteins and the flexibility of microtubules. Biochemistry 34:13374-13380.
8. Mickey, B., and J. Howard. 1995. Rigidity of microtubules is increased by stabilizing agents. J. Cell Biol. 130:909-917.
9. Pampaloni, F., G. Lattanzi, A. Jonáš, T. Surrey, E. Frey, and E.-L. Florin. 2006. Thermal fluctuations of grafted microtubules provide evidence of a length-dependent persistence length. Proc. Natl. Acad. Sci. USA 103:10248-10253.
10. Van den Heuvel, M. G., M. P. de Graaff, and C. Dekker. 2008. Microtubule curvatures under perpendicular electric forces reveal a low persistence length. Proc Natl Acad Sci U S A 105:7941-7946.
11. Venier, P., A. C. Maggs, M. F. Carlier, and D. Pantaloni. 1994. Analysis of microtubule rigidity using hydrodynamic flow and thermal fluctuations [published erratum appears in J Biol Chem 1995 Jul 14;270(28):17056]. Journal of Biological Chemistry 269:13353-13360.
12. Schaap, I. A., C. Carrasco, P. J. de Pablo, F. C. MacKintosh, and C. F. Schmidt. 2006. Elastic response, buckling, and instability of microtubules under radial indentation. Biophys J 91:1521-1531.
13. de Pablo, P. J., I. A. Schaap, F. C. MacKintosh, and C. F. Schmidt. 2003. Deformation and collapse of microtubules on the nanometer scale. Phys Rev Lett 91:098101.
14. Caplow, M., and J. Shanks. 1996. Evidence that a single monolayer tubulin-GTP cap is both necessary and sufficient to stabilize microtubules. Molecular Biology of the Cell 7:663-675.
15. Molodtsov, M. I., E. A. Ermakova, E. E. Shnol, E. L. Grishchuk, J. R. McIntosh, and F. I. Ataullakhanov. 2005. A molecular-mechanical model of the microtubule. Biophys. J. 88:3167-3179.
16. Sept, D., and F. C. MacKintosh. 2010. Microtubule elasticity: connecting all-atom simulations with continuum mechanics. Phys. Rev. Lett. 104:018101.
17. Kis, A., S. Kasas, B. Babicacute, A. J. Kulik, Beno, icirc, W. t, G. A. D. Briggs, Sch, ouml, C. nenberger, S. Catsicas, Forr, oacute, and L. 2002. Nanomechanics of Microtubules. Phys. Rev. Lett. 89:248101.

18. Kasas, S., A. Kis, B. M. Riederer, L. Forró, G. Dietler, and S. Catsicas. 2004. Mechanical Properties of Microtubules Explored Using the Finite Elements Method. Chemphyschem 5:252-257.
19. Wang, H.-W., and E. Nogales. 2005. Nucleotide-dependent bending flexibility of tubulin regulates microtubule assembly. Nature 435:911-915.
20. Hummer, G., and A. Szabo. 2005. Free Energy Surfaces from Single-Molecule Force Spectroscopy. Acc. Chem. Res. 38:504-513.
21. VanBuren, V., D. J. Odde, and L. Cassimeris. 2002. Estimates of lateral and longitudinal bond energies within the microtubule lattice. Proc Natl Acad Sci U S A 99:6035-6040.
22. Molodtsov, M. I., E. L. Grishchuk, A. K. Efremov, J. R. McIntosh, and F. I. Ataullakhanov. 2005. Force production by depolymerizing microtubules: a theoretical study. Proc Natl Acad Sci U S A 102:4353-4358.
23. Mandelkow, E. M., E. Mandelkow, and R. A. Milligan. 1991. Microtubule dynamics and microtubule caps: a time-resolved cryo-electron microscopy study. The Journal of Cell Biology 114:977-991.

Supplemental Figure Legends

Figure S1. Schematic demonstration of lateral shift and lateral rotation during the bond the transition.

Figure S2 Schematic illustration on how to calculate the gap width d_{gap} and kink position Γ from the force-indentation curve.

Figure S3 The calculated $\frac{\Delta U}{\Delta z_{MT}}$ v.s. z_{MT} from the simulations corresponding to Figure 2 (panel a) and Figure 4 (panel b-d). The gray area indicates the regions where the experiments and simulations are not under the same conditions.

Figure S4 Force V.S. Indentation curves for the L1 model (tube only model) at various ΔG_{Lat} based on the estimated values (-3.2~-5.7 k_BT (21)). The plots show the curves for (a) -3 k_BT; (b) -3.5 k_BT; (c) -4 k_BT; (d) -4.5 k_BT; (e) -5 k_BT; (f) -5.5 k_BT. The simulations produce either no observable gap, or the gap appears at a very high indentation value (>5

nm), with a short the second linear region. (g) The unzipping mechanism that gives rise to a gap in the F-I curves. The lateral bonds between blue colored tubulins are broken.

Figure S5 Effects of MT length on mechanical properties in the linear region. (a) One conformation of a 200 nm MT with energy plot under an AFM tip pressed at an indentation distance of 7.4 nm. Both the MT physical deformation and the energy changes indicate that the effects of the AFM tip can only be seen between z = 60 ~ 140 nm, which is about a 80 nm region along the MT. (b) The F-I curve for an AFM Tip Radius = 15 nm (upper panel) and 45 nm (lower panel), and MT length ~24 (circle), 40 (square), 80 (diamond) and 160 (triangle) nm, respectively. (c) Calculated κ versus MT length with AFM tip radius R = 15, 20, 25, 35, and 45 nm. (d) Calculated κ versus tip radius R with MT length = ~ 40, 80, 120, and 160 nm. (e) The gap starting position Γ versus MT length at AFM Tip radius R = 15, 20, 25, 35, and 45 nm.

Figure S6 Effects of AFM tip position shifting along both x (lateral direction, a-c) and z (longitudinal direction, d-f). (a) Selected MT configurations for tip center at the middle of the MT (z~=half of MT length) and x= 0 and -7 nm. (b) End-on view of part of the MT wall before the AFM tip reaches the wall. The AFM tip is pressed down along the negative y direction. When the starting position of the AFM tip moves from x=0 toward negative x direction, monomers 1, 2 and 3 contacts the AFM tip sequentially. (c) Spring constant κ (slope of linear region of Force v.s. Indentation curve) v.s. shift distance along x direction of AFM tip (Δd_x). Inset: zoomed in plot for κ at $-5.5 \le \Delta d_x \le -3$ nm. (d) Γ(recorded first kink position on Force v.s. Indentation curve) v.s. Δd_x . (e) Several MT conformations at indentation = 7 nm for Tip Position change from central = 0, 40, and 80 nm. (f) Spring constant κ (Slope of linear region of Force v.s. Indentation curve) v.s.

shift distance along z direction of AFM tip from the middle of the MT (Δd_z). (g) Γ (The recorded first kink position) v.s. Δd_z .

Figure S7 Illustration of the coupled system of cantilever and MT wall. The cantilever is treated as linear spring and the MT wall is a non-linear spring. z_S is defined as the deformation of cantilever spring, z_{AFM} is the upper position of cantilever, z_{MT} is the upper position of MT wall. The lower position of the MT wall is immobilized on the glass. The left panel represents the relaxed status of the system and the right panel represents the status with force exerted on it.

Figure S8 Simulated tip structure for disassemble stage for L2 model.

Figure S9 The Parameter sensitivity analysis on "gap" behavior for Tube-only model. A) the slope contour; b) the Kink position contour. The parameters producing non-physical values are washed out. The overlaps of A and B are parameters which can generate both linearly reasonable response and kink like behavior.

Microtubules	Methods	Flexural Rigidity (x 10^{-24} Nm^2)	Temperature (^0C)	References
Pure MT	Buckling force	7.9	33	(5)
	Hydrodynamic flow	8.5	37	(11)
	Hydrodynamic flow	35.8	37	(7)
	Relaxation (RELAX)	3.7	22-25	(3)
	Relaxation (WIGGLE)	4.7	22-25	(3)
	Thermal fluctuation	26.0	37	(8)
	Thermal fluctuation	4.6	37	(11)
	Thermal fluctuation	26.5*	37	(7)
	Thermal fluctuation	18.5		(2)
	Thermal fluctuation	13.7-27.0*	23	(4)
Paclitaxel-stabilized MT	Buckling force	2.0	33	(5)
	Buckling force	2.0-22	37	(6)
	Relaxation (RELAX)	1.0	22-25	(3)
	Relaxation (WIGGLE)	1.9	22-25	(3)
	Thermal fluctuation	21.5	25	(3)
	Thermal fluctuation	32.0	37	(8)
	Thermal fluctuation	2.4	37	(11)
	Thermal fluctuation	0.47~21.5*[+]	37	(9)
	Electric force	0.34*[#]	37	(10)

*These values of EI were derived from measured persistence length l_p with $EI = k_B T \cdot l_p$.

[+]the corresponding MT length is 2.6~47.5 μm.

[#]the MT length is ~0.1 μm

Table S1 Flexural Rigidity Measurements

Fig S1

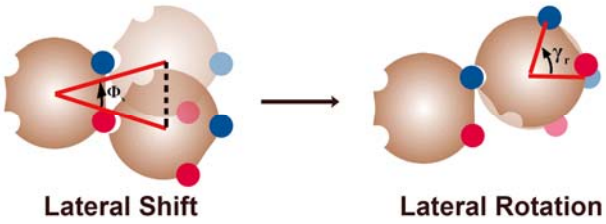

Fig S2

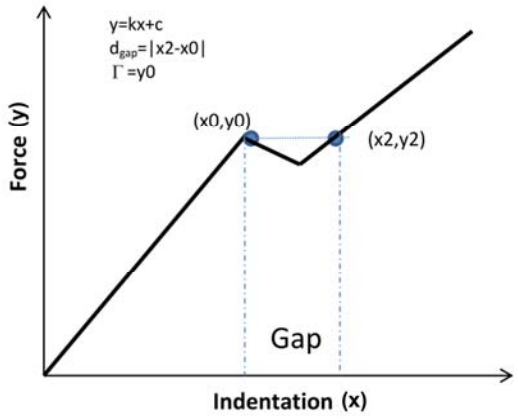

Fig S3

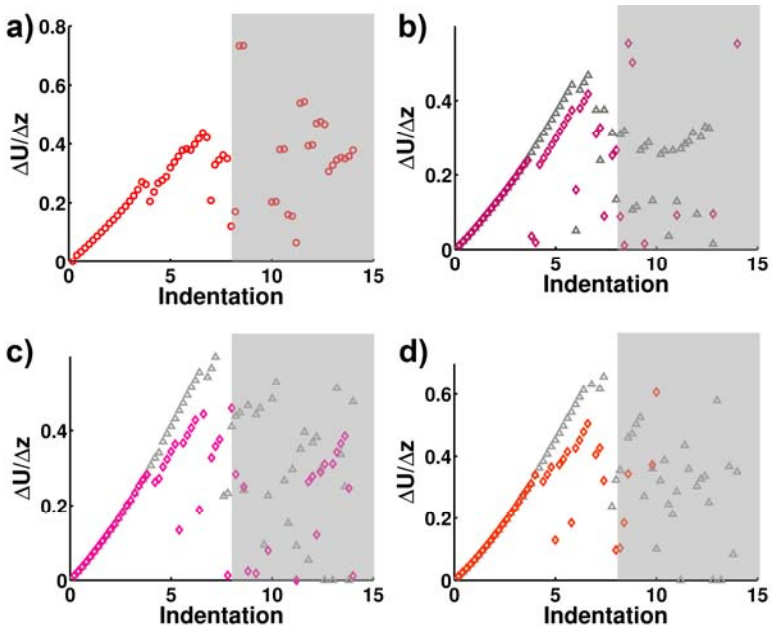

Fig S4

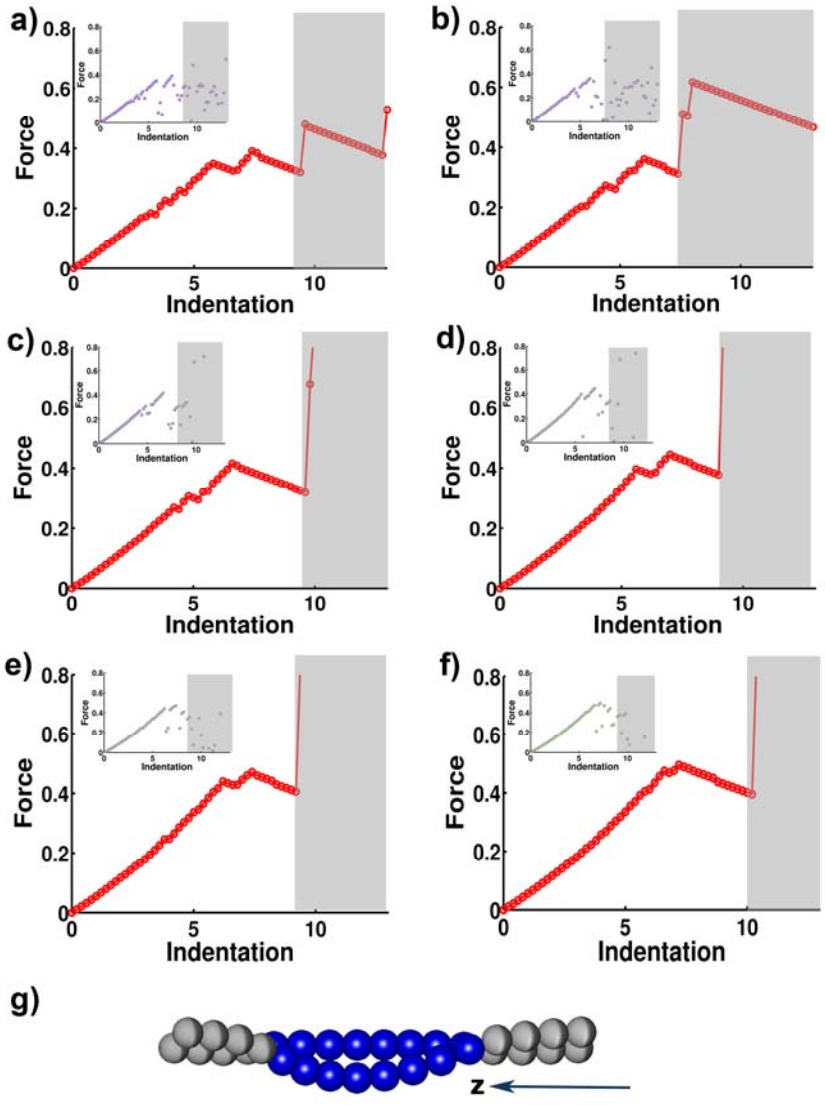

Fig S5

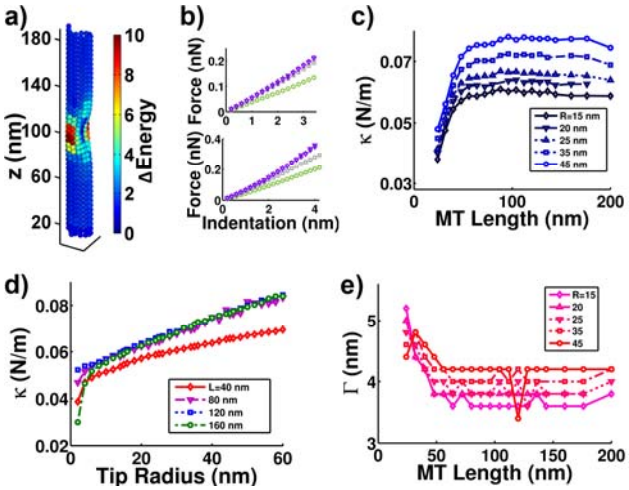
a)
b)
c)
d)
e)
z (nm)
ΔEnergy
Force (nN)
Indentation (nm)
κ (N/m)
MT Length (nm)
Rs=15 nm
20 nm
25 nm
35 nm
45 nm
Tip Radius (nm)
Ls=40 nm
80 nm
120 nm
160 nm
Γ (nm)

Fig S6

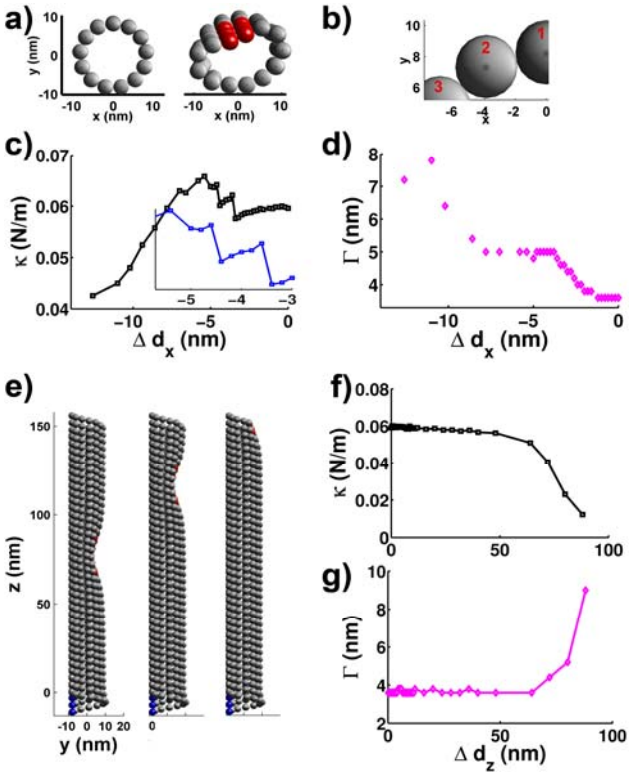

Fig S7

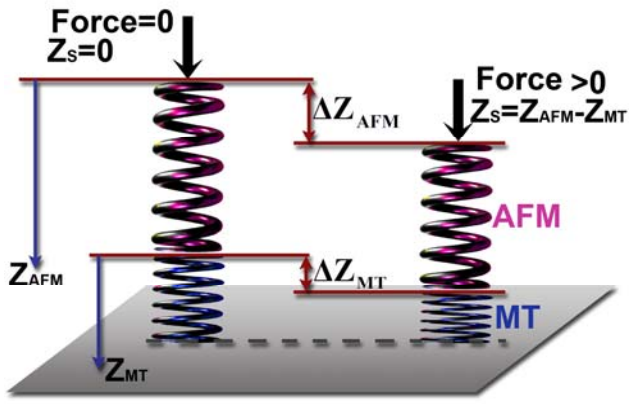

Fig. S8

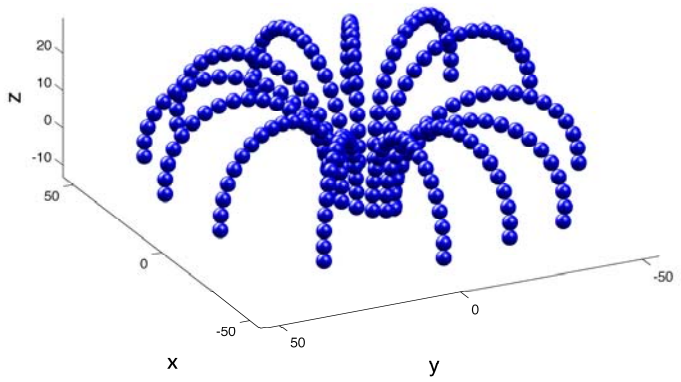

Fig. S9

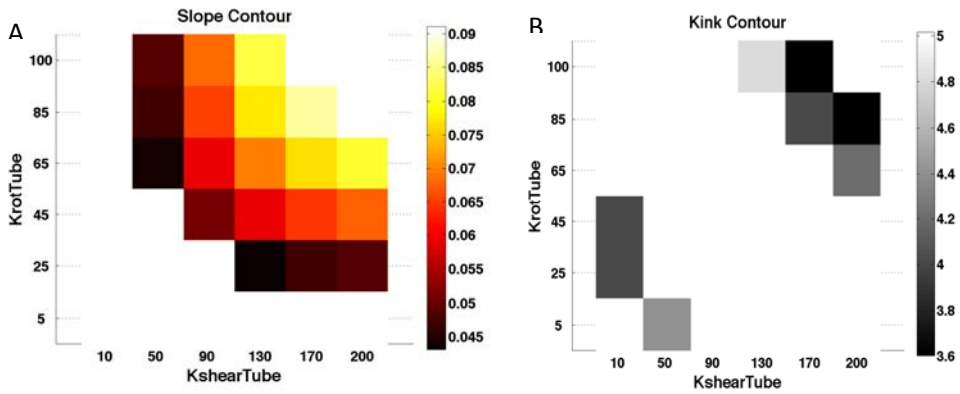
A
Slope Contour
KrotTube
KshearTube
100
85
65
45
25
5
10
50
90
130
170
200
0.09
0.085
0.08
0.075
0.07
0.065
0.06
0.055
0.05
0.045
B
Kink Contour
KrotTube
KshearTube
100
85
65
45
25
5
10
50
90
130
170
200
5
4.8
4.6
4.4
4.2
4
3.8
3.6